

A COMPUTATIONAL STUDY SUMMARIZING THE EFFECTS OF COMPOSITION ON THE MELT POOL GEOMETRY IN ADDITIVE MANUFACTURING

Daniel Gwynn¹, Sree Samhita Gundimedda², Nandana Menon¹, and Amrita Basak^{1,*}

¹Department of Mechanical Engineering, The Pennsylvania State University,
University Park, PA 16802, USA

² Green Valley School, Near Airforce Campus, Lekawada,
Gujarat 382042, India

* Communicating Author: aub1526@psu.edu

Abstract

Thermophysical properties play a crucial role in controlling the melt pool dimensions in metal additive manufacturing (AM). It is, therefore, imperative to understand the impact of thermophysical properties on the melt pool dimensions for critical materials such as nickel-based superalloys. In this paper, a three-dimensional analytical model is used to predict the steady-state melt pool dimension over a range of process parameters for several nickel-based superalloys. The effects of composition, in terms of the thermophysical properties, on the melt pool dimensions are also studied. The results show that the melt pool dimensions correlate well with the liquidus temperature, density, and thermal conductivity of the alloy. By exploring the impact of process parameters and compositions on the melt pool dimension evolution, a framework can be established to maintain the desired melt pool dimensions during the fabrication of functionally-graded parts with different alloys belonging to the same material class.

Introduction

Nickel-based superalloys are widely used in the production of gas-turbine hot-section as they provide higher yield strength with increasing operating temperatures partly due to the presence of secondary γ' phases [1]. The hot-section components are manufactured using conventional manufacturing methods such as investment casting. However, the fabrication of complex designs and functionally-graded components is not feasible using such conventional techniques. Additionally, repair of the superalloy components using conventional methods is challenging as they are difficult to weld. By addressing both these constraints, metal additive manufacturing (AM) presents itself as a viable solution.

Metal AM works on the principle of consolidating metallic feedstocks (e.g., wire or powder) in layers using a high-energy heat source (e.g., a laser, an electron beam, or an arc). Understanding the fundamental physics of metal AM is a critical requirement for process development, optimization, and control [2]. The heat source in metal AM (e.g., powder bed fusion, directed energy deposition) creates a small melt pool that controls the microstructures and, therefore, the mechanical properties of the final part [3]. This makes melt pool geometry a critical parameter in metal AM. Numerous studies involving the modeling and simulation of the melt pool geometry in metal AM processes for nickel-based alloys are available in literature. Analytical

models are extensively used to model the melt pool geometry for nickel-based superalloys. Gäumann [4] used a modified Rosenthal solution [5] to obtain the liquid isotherm and a circular melt pool. Christensen et al. [6] suggested an elliptic melt pool along the direction of the beam's movement. Goldak et al. [7] assumed a double-ellipsoid weld pool shape that consisted of front and rear ellipsoid quadrants. Wang et al. [8] developed a finite element model expanded to include an intensity distribution for estimating the melt pool dimensions of CMSX-4[®]. More recently, Mondal et al. [9] developed a Gaussian Process-based regression model to predict the melt pool geometry for a popular nickel-based superalloy, CMSX-4[®].

In addition to analytical models, Finite Element Methods (FEM) and Finite Volume Methods (FVM) are also used for predicting the melt pool geometry in metal AM of nickel-based superalloys [10]. A computational fluid dynamics (CFD)-based model allows the incorporation of fluid convection inside the melt pool. To accurately simulate the condition inside the melt pool, surface tension-driven flow known as the Marangoni convection (or Bernard-Marangoni convection) needs to be included in the flow-thermal model [3]. A liquid with a higher surface tension pulls more strongly on the surrounding liquid than the one with lower surface tension. This extends the melt pool laterally and makes it shallower. Acharya et al. [3] developed a three-dimensional CFD model and obtained good agreement with experimental data for the melt depth in CMSX-4[®] processed through powder bed fusion. A 2D approach was also implemented to simulate the melt pool characteristics for IN100 and obtained a reasonably good agreement for the melt depth and the average melt temperature [11]. This model was also extended by Basak et al. [12] to simulate melt pool characteristics for CMSX-4[®] with reasonable congruence between the simulation and the experimental results achieved for the melt depth and the average melt pool temperature.

While several studies outline the effects of processing parameters on the melt pool geometry, there exists a knowledge gap in the exploration of the combined effects of the composition of nickel-based superalloys and process parameters on the melt pool geometry. This paper attempts to evaluate the effects of both composition and process parameters on the melt pool geometry of several different nickel-based superalloys. An analytical model presented by Eagar-Tsai [13] is utilized for predicting the melt pool geometry. The model is thoroughly validated using the literature data. Thereafter, several popular nickel-based superalloys are selected, and their thermo-physical properties are evaluated using JMatPro[®] [14]. The Eagar-Tsai analytical model is, thereafter, interrogated to evaluate the effects of composition and process parameters on the steady-state melt pool geometry (e.g., depth). The results show that the melt pool dimensions correlate well with the liquidus temperature, density, and thermal conductivity of the alloy. By exploring the impact of process parameters and compositions on the melt pool dimension evolution, a framework can be established to maintain the desired melt pool dimensions during the fabrication of functionally-graded parts with different alloys belonging to the same material class.

Methods

This section, first, provides a brief description of the analytical model. Thereafter, the model is validated against two sets of experimental results.

Analytical Model

The analytical model selected in this work was originally developed by Eagar and Tsai [13]. This model is based on Rosenthal’s steady-state model. However, the model also uses a more realistic Gaussian beam power source instead of Rosenthal’s point source. Except for a point source and steady-state conditions, Rosenthal’s original assumptions remain intact [5]. Eagar-Tsai’s model starts with the following equation:

$$T - T_0 = -\frac{q}{2\pi kR} e^{-\frac{v(w+R)}{2a}} \tag{1}$$

Here, T is the temperature ($^{\circ}\text{C}$), T_0 is the initial temperature ($^{\circ}\text{C}$), q is the input power (W), k is the thermal conductivity ($\text{W}/(\text{m}^{\circ}\text{C})$), R (m) is the distance from the heat source defined as $(w^2 + y^2 + z^2)^{1/2}$, v is the power source travel speed (m/s), w is the distance (m) in the x -direction in a moving coordinate of speed v defined as $x - vt$, and a is the thermal diffusivity (m^2/s). Eagar-Tsai’s model expands the above equation as follows:

$$T - T_0 = \int_0^t dt'' \left[\frac{q(t'')^{-1/2}}{\pi\rho c(4\pi a)^{1/2}(2at'' + \sigma^2)} \right] \left[e^{-\frac{w^2+y^2+2wvt+v^2t''^2}{4} - \frac{z^2}{4at''}} \right] \tag{2}$$

Here, t is the time (s), t'' is the superposed time (s), ρ is the density (kg/m^3), c is the specific heat ($\text{J}/(\text{kg } ^{\circ}\text{C})$), and σ is the beam distribution parameter (m). The coordinate system utilized in this model is illustrated in Figure 1(A). Figure 1(B) illustrates the definitions of melt pool depth, length, and width used in the present research.

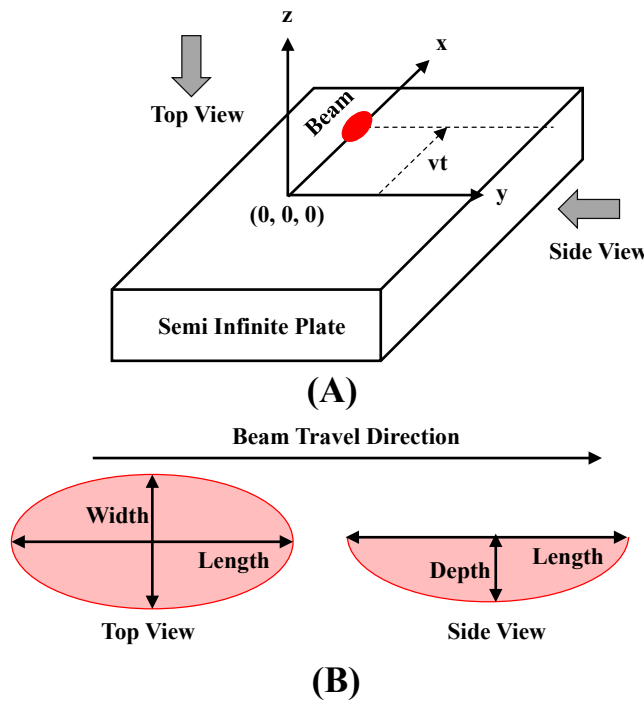


Figure 1. (A) Schematic of the coordinate system used in the analytical model and (B) Definition of the melt pool depth, length, and width.

This model's primary assumptions include the following:

- Convective and radiative heat transfer mechanisms are ignored.
- The thermal properties of the material are constant.
- The computational domain is semi-infinite.
- The phase change of the material is not included.

Despite its limitations, Eagar-Tsai's model is extensively used for parameter space exploration through the design-of-experiments (DoE)-based approaches [9]. Computationally efficient surrogates have also been developed using this model for AM applications [9].

Validation of the Analytical Model

This section summarizes the validation results obtained using two different sources of experimental data. In the first validation, the melt pool measurements reported by Ning et al. [15] for Inconel 625 are utilized. Three different process parameter combinations are selected: Case 1 with power, $P = 169$ W and laser scan speed, $v = 875$ mm/s; Case 2 with $P = 182$ W and $v = 800$ mm/s, and Case 3 with $P = 195$ W and $v = 800$ mm/s. Here, P is calculated as $\eta \times q$ where η is the laser absorptivity coefficient. Utilizing $\eta = 0.4$, an average error of 4.3% with a maximum error of 7.3%, and a minimum error of 1.5%, are observed for the melt pool length and depth when compared with the results reported by Ning et al. The results of this validation are shown in Figure 2.

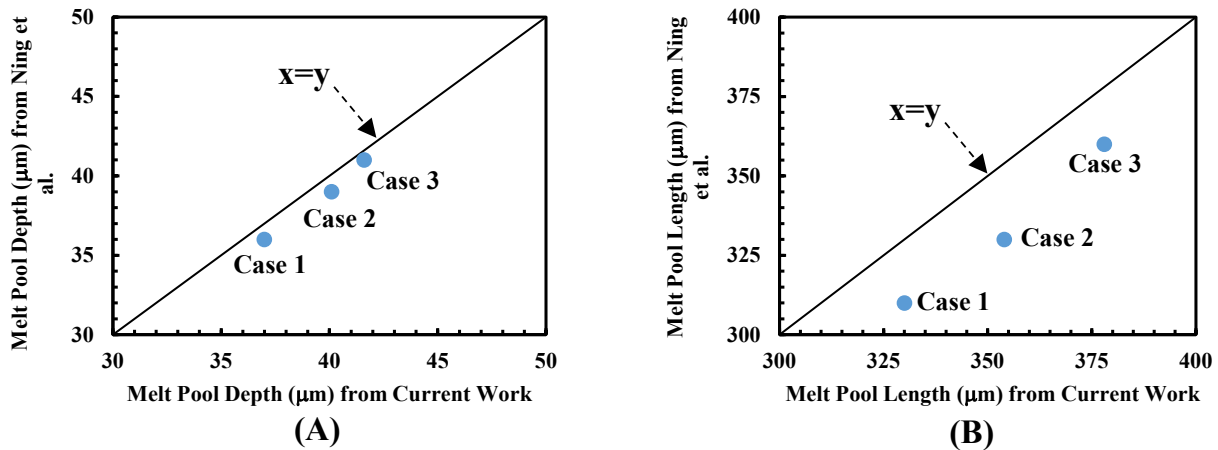


Figure 2. Validation results (A) for melt pool depth and (B) melt pool length using measurements from Ning et al. [14].

For the second validation, the melt pool measurements recorded for CMSX-4[®] by Anderson et al. [10] are utilized. Results are obtained for Case 1: $P = 240$ W and $v = 1$ mm/s; Case 2: $P = 240$ W and $v = 6$ mm/s; Case 3: $P = 360$ W and $v = 1$ mm/s; and Case 4: $P = 360$ W and $v = 6$ mm/s. The results of this validation are illustrated in Figure 3. This validation results in a maximum error of 21.5%, and a minimum error of 1.0%, cumulating to an average error of 9.4%.

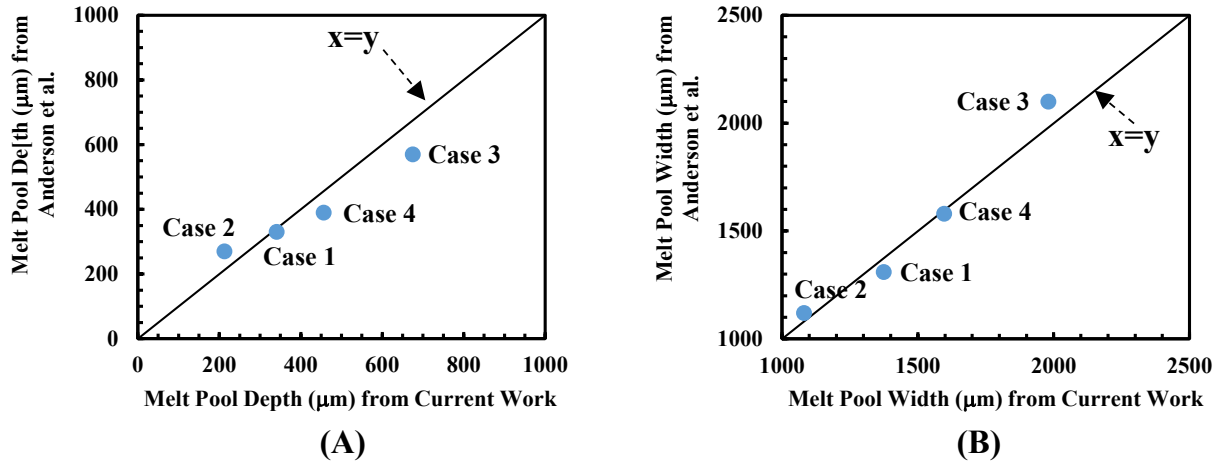


Figure 3. Validation results (A) for melt pool depth and (B) melt pool width using measurements from Anderson et al. [10].

Results and Discussion

Effects of Composition

Ten different superalloy materials are selected in this paper whose compositions are given in Table 1 [16].

Table 1. Composition (in Wt. %) of the ten alloys considered in this work.

	B 1900	CMSX- 4[®]	GTD 444	IN 100	Mar M 200+Hf	Mar M-002	PWA- 1426	PWA 1484	Rene N6	SR- 99
C	0.1	-	0.1	0.16	0.14	0.15	0.1	-	-	-
Cr	8	6.5	9.75	10	9	9	6.5	5	4	8
Ni	Bal	Bal	Bal	Bal	Bal	Bal	Bal	Bal	Bal	Bal
Co	10	9	7.5	15	10	10	12	10	12	5
Mo	6	0.6	1.5	3	-	-	2	1.9	1	-
W	-	6	6	-	12	10	3	5.9	6	10
Nb	-	-	-	-	1	-	-	-	-	-
Ta	4.25	6.5	4.8	-	-	2.5	4	8.7	7	3
Ti	1	1	3.6	4.75	2	1.5	-	-	-	2.2
Al	6	5.6	4.23	5.5	5	5.5	6	5.65	5.8	5.5
B	0.015	-	-	0.015	0.015	0.015	0.015	-	-	-
Zr	0.07	-	-	0.04	-	0.05	0.03	-	-	-
Hf	-	0.1	-	-	0.8-1.9	1.5	1.5	0.1	0.2	-
Re	-	3	-	-	-	-	3	3	5	-
Y	-	-	-	-	-	-	-	0.013	-	-

The thermophysical properties are determined using JMatPro[®] [14] and average values are determined for ρ , k , a , and c at 300 K. These properties are recorded in Table 2.

Table 2. Material properties of composition of ten alloys selected in Table 1. Here ρ in (kg/m^3), a in ($\text{m}^2/\text{s} \times 10^{-6}$), k in ($\text{W}/(\text{m}^\circ\text{C})$), c in ($\text{J}/(\text{kg}^\circ\text{C})$), T_L in ($^\circ\text{C}$)

	B1900	CMSX-4[®]	GTD 444	IN 100	Mar M 200 + Hf	Mar M 002	PWA 1426	PWA 1484	Rene N6
ρ	8720	8592	8488	7871	8559	8563	8487	8770	8926
a	3.14	3.24	3.12	3.15	3.33	3.32	3.41	3.28	3.44
k	11.97	11.90	11.09	11.34	11.97	11.94	12.54	11.99	12.45
c	436.78	426.62	418.60	455.95	419.43	419.01	432.06	416.26	405.52
T_L	1354	1379	1354	1351	1376	1356	1384	1379	1401

To highlight the effect of process parameters, three different combinations of laser power, P , and scan velocity, v , are studied for a representative alloy, PWA-1426. The cases presented here are - Case A: $P = 900$ W and $v = 2$ mm/s; Case B: $P = 900$ W and $v = 6$ mm/s; and Case C: $P = 450$ W and $v = 6$ mm/s. The process parameter values are selected to account for the melt pool development under a combination of high and low P, v values.

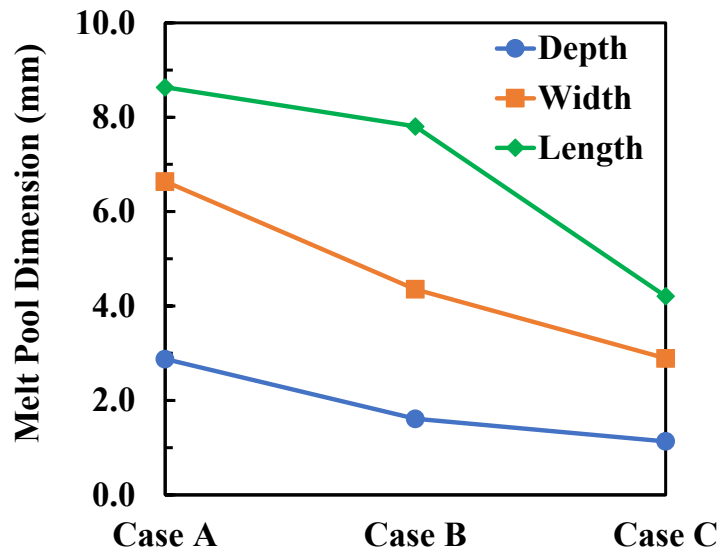


Figure 4. Variation of melt pool dimensions (depth, width, and length) for PWA-1426.

The melt pool dimensions for each case are plotted in Figure 4. There is a clear influence of both P and v on the melt pool geometry – a larger melt pool is observed for higher P values while higher values of v inhibit the size of the melt pool. Additionally, amongst the three melt pool dimensions, the melt pool length appears to be the most influenced by a change in process

parameters. With this preliminary understanding of the impact of process parameters, the melt pool dimensions are analyzed over the range of alloys differing in composition, at constant P and v . Figure 5 shows the depth variation of all ten alloys for Case B: $P = 900$ W and $v = 6$ mm/s. The results show that for the same processing parameters, GTD 444 has the largest melt pool dimensions while SR-99 has the smallest with the difference in the melt pool depth, length, and width being 6%, 25%, and 12%, respectively.

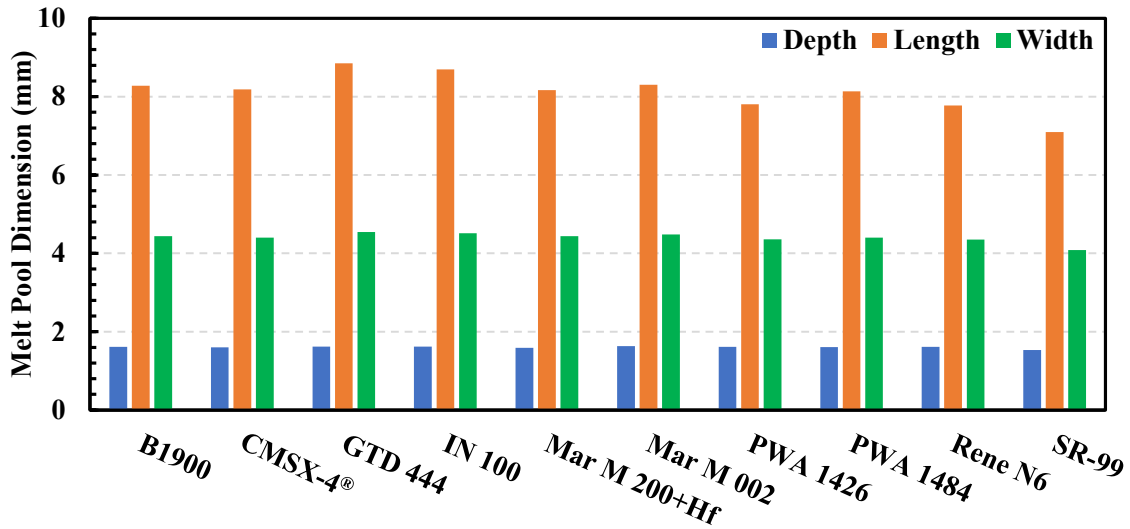


Figure 5. Variation of melt pool dimensions for ten alloys processed at Case B: $P = 900$ W and $v = 6$ mm/s.

To understand the differences in the melt pool dimension with composition, the melt pool dimension (depth) is studied as a response to the thermo-physical properties of all ten alloys as investigated in Figure 5. These results are consolidated in Figure 6. Figure 6(A) shows the variation of the melt pool depth with the liquidus temperature, T_L . The results show a significant negative correlation with T_L . The temperature is the highest near the laser source and decreases away from the laser source. Since the definition of the melt pool boundary is the iso-surface of the liquidus temperature, a lower liquidus temperature would imply that the melt pool boundary would lie further away from the laser source, thereby, increasing the melt pool depth. Figures 6(B) and (C) illustrate the variation of melt pool depth with density, ρ , and thermal conductivity, k , respectively. For an identical laser power, the material with a lower density would have a higher volumetric heat flux which would, in turn, increase the melt pool depth. The effects of the thermal conductivity are observed to have the most prominent influence on the ten alloys tested. With an increase in thermal conductivity, the melt pool gets elongated, due to an improved heat flow via conduction. This reduces the penetration and hence the melt pool depth is smaller with an increase in thermal conductivity.

Similar plots are also made to investigate the effects of the specific heat, c , and the thermal diffusivity, a , on the melt pool depth as shown in Figures 6(D) and (E). However, no correlations are observed between the specific heat and the thermal diffusivity. One would expect the influence of thermal diffusivity to be prominent due to an improved heat flow via diffusion which would increase the area of the melt pool along the scan direction and, hence, decrease the melt pool depth. The specific heat controls the rate at which the material would respond to heat flux thereby

suggesting a lower specific heat may contribute to an increase in the melt pool size. Models of higher fidelity are, thus, required to capture the relationship between the thermophysical properties and melt pool with better accuracy and reliability.

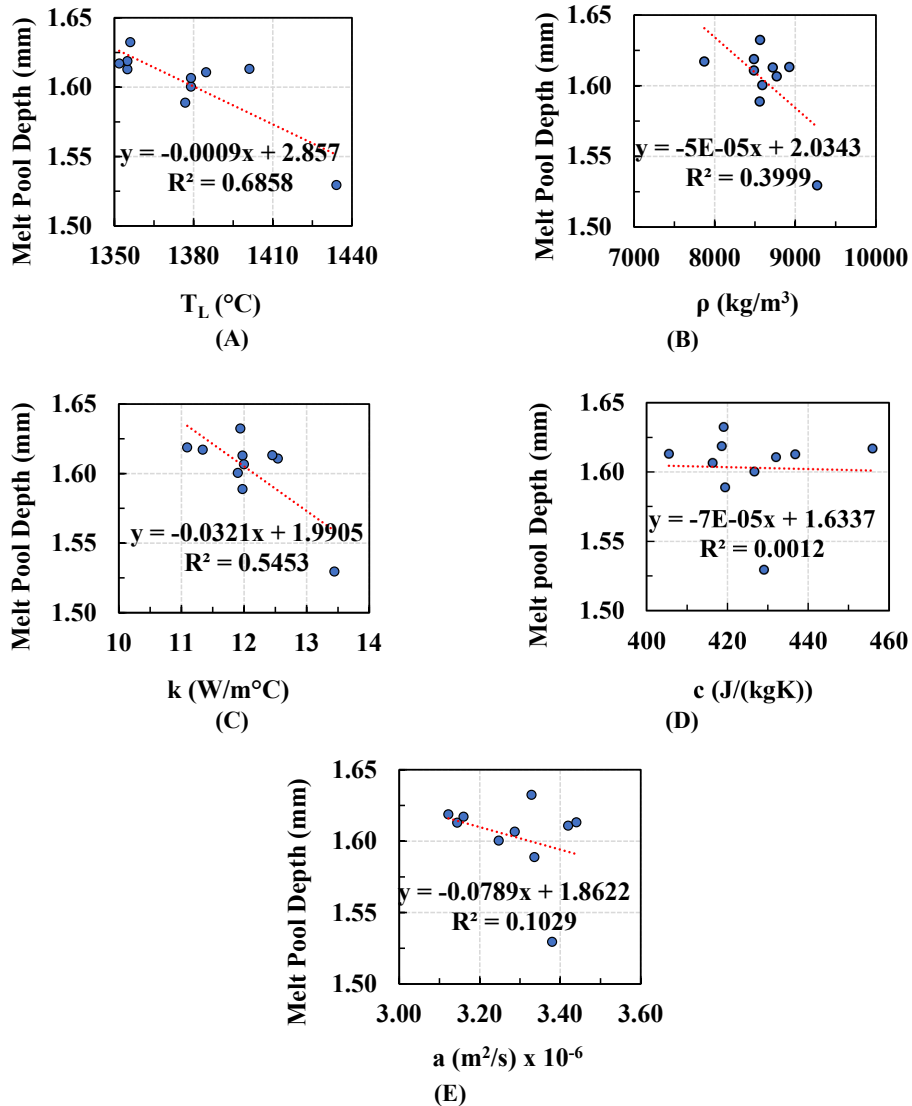


Figure 6. Variation of melt pool depth with (A) T_L , (B) ρ , (C) k , (D) c , and (E) a . The dotted linear fit and R^2 values are also indicated on each plot.

The p values for the regressions are also reported in Table 3. The small p values ($< .05$) for T_L , ρ and k also confirm the significance of predictions. However, both specific heat and thermal diffusivity do not appear to be significant ($p > .05$) for the ranges evaluated. This gives an important insight into what variables are critical. E.g., While building predictive models for melt pool geometry, specific heat and thermal diffusivity could be avoided. Including non-significant variables can affect the accuracy and increase the dimensionality of the input space, thereby requiring more data.

Table 3. p values reported for the linear regression.

Variable \ Term	Coefficient	Variable
T_L	0	.001
ρ	0	.05
k	0	.015
c	.001	.923
a	0	.366

Conclusion

A three-dimensional analytical melt pool model based on the work of Eagar-Tsai is developed and validated with results reported by Ning et al. and Anderson et al. with predictions resulting in average errors of 4.3% and 9.4%, respectively. These results are obtained after appropriate calibration of the beam distribution parameter and/or the laser absorptivity coefficient. The model is interrogated to evaluate the effects of the thermophysical properties resulting from the different alloy compositions on the melt pool dimension. The melt pool dimensions show significant correlations with density, liquidus temperature, and thermal conductivity. It is anticipated that this model can provide the desired fidelity for quick screening of alloy compositions and process parameters.

While the developed model can provide sufficiently accurate results, its accuracy may be improved by including additional parameters at the cost of added complexity. Some of these additions that would be expected to improve model accuracy include using temperature-based thermophysical material properties, including provisions for finite dimensions, incorporating convective and radiative heat transfer, and adding latent heat effects due to phase change. In the future, surrogate models [9] will be developed over a wide range of alloy compositions. Since the alloy composition is a high-dimensional space (i.e., the number of elements in an alloy is fifteen or more), suitable dimensional reduction methodologies need to be implemented. The Eagar-Tsai model is not accurate. To improve the accuracy of the prediction, multi-fidelity surrogates will also be developed [17].

Acknowledgments

The work reported in this paper is supported by the Department of Mechanical Engineering at the Pennsylvania State University, University Park, PA 16802. Nandana Menon would like to acknowledge the James E. Marley Fellowship, the Kulakowski Travel Grant awarded by the Mechanical Engineering Department of the Pennsylvania State University, and the National Science Foundation Student Support offered by the organizing committee of the Solid Freeform Fabrication Symposium. Any opinions, findings, and conclusions in this paper are those of the authors and do not necessarily reflect the views of the supporting institutions.

References

- [1] N. M. Angel and A. Basak, "On the Fabrication of Metallic Single Crystal Turbine Blades with a Commentary on Repair via Additive Manufacturing," *J. Manuf. Mater. Process.*, vol. 4, no. 4, p. 101, Oct. 2020.
- [2] A. Basak and S. Das, "Epitaxy and microstructure evolution in metal additive manufacturing," *Annu. Rev. Mater. Res.*, vol. 46, pp. 125–149, 2016.
- [3] R. Acharya, R. Bansal, J. J. Gambone, and S. Das, "A Coupled Thermal, Fluid Flow, and Solidification Model for the Processing of Single-Crystal Alloy CMSX-4 Through Scanning Laser Epitaxy for Turbine Engine Hot-Section Component Repair (Part I)," *Metall. Mater. Trans. B*, vol. 45, no. 6, pp. 2247–2261, 2014.
- [4] M. Gäumann, S. Henry, F. Cleton, J.-D. Wagniere, and W. Kurz, "Epitaxial laser metal forming: analysis of microstructure formation," *Mater. Sci. Eng. A*, vol. 271, no. 1–2, pp. 232–241, 1999.
- [5] D. Rosenthal, "Mathematical theory of heat distribution during welding and cutting," *Weld. J.*, vol. 20, pp. 220–234, 1941.
- [6] N. Christensen, "Distribution of temperatures in arc welding," *Brit. Weld. J.*, vol. 12, no. 2, 1965.
- [7] J. Goldak, A. Chakravarti, and M. Bibby, "A new finite element model for welding heat sources," *Metall. Trans. B*, vol. 15, no. 2, pp. 299–305, 1984.
- [8] G. Wang, J. Liang, Y. Zhou, T. Jin, X. Sun, and Z. Hu, "Prediction of Dendrite Orientation and Stray Grain Distribution in Laser Surface-melted Single Crystal Superalloy," *J. Mater. Sci. Technol.*, vol. 33, no. 5, pp. 499–506, 2017.
- [9] S. Mondal, D. Gwynn, A. Ray, and A. Basak, "Investigation of Melt Pool Geometry Control in Additive Manufacturing Using Hybrid Modeling," *Metals*, vol. 10, no. 5, 2020.
- [10] T. D. Anderson, J. N. DuPont, and T. DebRoy, "Origin of stray grain formation in single-crystal superalloy weld pools from heat transfer and fluid flow modeling," *Acta Mater.*, vol. 58, no. 4, pp. 1441–1454, 2010.
- [11] R. Acharya and S. Das, "Additive Manufacturing of IN100 Superalloy Through Scanning Laser Epitaxy for Turbine Engine Hot-Section Component Repair: Process Development, Modeling, Microstructural Characterization, and Process Control," *Metall. Mater. Trans. A*, vol. 46, no. 9, pp. 3864–3875, 2015.
- [12] A. Basak, R. Acharya, and S. Das, "Additive Manufacturing of Single-Crystal Superalloy CMSX-4 Through Scanning Laser Epitaxy: Computational Modeling, Experimental Process Development, and Process Parameter Optimization," *Metall. Mater. Trans. A*, vol. 47, no. 8, pp. 3845–3859, Aug. 2016.
- [13] T. W. Eagar and N. S. Tsai, "Temperature fields produced by traveling distributed heat sources," *Weld. J.*, vol. 62, no. 12, pp. 346–355, 1983.
- [14] "Sente Software - JMatPro®." [Online]. Available: <https://www.sentesoftware.co.uk/jmatpro>. [Accessed: 25-Nov-2020].
- [15] J. Ning, D. E. Sievers, H. Garmestani, and S. Y. Liang, "Analytical Modeling of In-Process Temperature in Powder Bed Additive Manufacturing Considering Laser Power Absorption, Latent Heat, Scanning Strategy, and Powder Packing," *Mater. (Basel, Switzerland)*, vol. 12, no. 5, p. 808, Mar. 2019.
- [16] "Cannon Muskegon." [Online]. Available: <https://cannonmuskegon.com/>. [Accessed: 20-Apr-2022].

- [17] N. Menon, S. Mondal, and A. Basak, “Multi-Fidelity Surrogate-Based Process Mapping with Uncertainty Quantification in Laser Directed Energy Deposition,” *Materials (Basel)*., vol. 15, no. 8, p. 2902, Apr. 2022.